OMAE2020-18605

NUMERICAL MODELLING OF THE INTERACTION OF MOVING FISH NETS AND FLUID

Tobias Martin[*]
Marine Civil Engineering
Department of Civil and Environmental Engineering
Norwegian University of Science and Technology
7491 Trondheim, Norway
Email: tobias.martin@ntnu.no

Gang Wang
Hans Bihs
Marine Civil Engineering
Department of Civil and Environmental Engineering
Norwegian University of Science and Technology
7491 Trondheim, Norway

ABSTRACT

The significant difference in length scales between the flow around a moving fish net and the flow around each twine of the net prevents the resolution of the complete structure within a discrete fluid domain. In this paper, this issue is overcome by calculating the net and fluid dynamics separately and incorporate their interaction implicitly. The forces on the net are approximated using a screen force model, and the motion of the net is computed with a lumped mass method. Here, a linear system of equations is derived from the dynamic equilibria and kinematic relations. The net model is coupled to the CFD solver REEF3D which solves the incompressible Navier-Stokes equations using high-order finite differences in space and time. Several numerical calculations are provided, and the comparison of loads and velocity reduction with available measurements indicates the good performance of the proposed model.

INTRODUCTION

Offshore aquaculture has seen growing interest due to greater concern regarding traditional aquaculture and its environmental impact on coastal regions. In the past, the design process was mostly based on the assumption that a decoupled consideration of fluid dynamics and structural deformation is valid. Løland [1] utilised linearised turbulent wake equations to approximate the

wake velocity behind the net, whereas other research relied on solutions from potential theory as wave input [2]. A separated approach of investigating the fluid and structural system loses validity under consideration of the changing environment offshore and the steadily increasing structure size because of the strong relationship between the motion of the structure and its interaction with the net. Therefore, coupled numerical simulations using less restrictive equations to describe the physical interaction become relevant. Here, the structural response and the disturbance of the fluid is directly determined from time-dependent fluid dynamics in and around the cage.

The significant difference in length scales between the flow around the fish cage and the flow around each twine of the net prevents the resolution of the complete structure within a discrete fluid domain. To overcome this issue, the calculation of net and fluid dynamics are separated and their interaction is incorporated using a coupling algorithm. Recently, a porous medium model was developed which defines a porous medium around the net. The governing volume- and Reynolds-averaged Navier-Stokes equations are solved using a finite volume method [3–5]. Chen and Christensen [6, 7] derived more advanced porous resistance coefficients to account for the porosity of the net. In Martin et al. [8], this approach was validated for fixed and moving net sheets in steady current flow. In this paper, an alternative method is utilised which is based on Lagrangian-Eulerian considerations which are generally efficient and applicable. Further, a screen

---

[*]Address all correspondence to this author.

force model [9] is implemented to account for the hydrodynamic forces on the net and the disturbances from the solid parts of the porous structure are distributed in the fluid domain using a continuous forcing approach.

Most numerical models for simulating the dynamics of nets are based on simplified finite element methods [10] or lumped mass methods [11]. In lumped mass methods, the net is discretised into multiple knots connected with elastic and massless bars. The solution is sought for the accelerations of the knots by solving Newton's second law and explicit time integration is applied to obtain the velocities and positions of the knots afterwards. This approach was successfully coupled to a porous medium model to simulate the interaction of flexible net sheets [4] and net cages [12] with steady fluid. The disadvantages arising from the explicit time integration and missing constitutive equations led to the development of implicit dynamic methods. In [13], an implicit quasi-static net model was introduced. High efficiency is given due to missing time step restriction, but the approach lacks justification for applications including large motions and snap loads due to increased accelerations between fluid and net motion. A more elaborated approach is provided in [14] where a dynamic net model based on a similar proposition was presented. The original method suffers from an inelastic material assumption which led to the development of the implicit net model of Marichal [15]. This approach is also the chosen net model in this paper.

The net model is implemented in the open-source Computational Fluid Dynamics (CFD) code REEF3D [16]. The code has been used and validated for a wide range of marine applications, such as breaking kinematics [17], breaking wave forces [18], sloshing [19] and fluid-structure interaction of floating objects [20, 21]. The new contribution of this paper consists of the development of a dynamic implicit net model and its coupling to a CFD fluid solver for calculating the interaction with the fluid. Thus, it is possible to analyse the deformation of nets in complex fluid conditions.

In the following, details about the numerical fluid and net models, as well as their coupling, are presented. Afterwards, validation cases for the coupling algorithm, the net motion and the fluid-structure interaction are provided. The comparison of loads on and velocity reductions behind a fixed and moving net panel with available measurements indicates the good performance of the proposed model. Additionally, four moving net panels are presented in order to emphasise the computational efficiency of the implementation.

NUMERICAL MODEL FOR SOLVING FLUID DYNAMICS

The basis for the presented developments is the open-source CFD solver REEF3D. In this framework, the continuity and Navier-Stokes equations are solved in the whole domain:

$$\nabla \cdot \mathbf{u} = 0, \tag{1}$$

$$\frac{\partial \mathbf{u}}{\partial t} + \mathbf{u} \cdot \nabla \mathbf{u} = -\frac{1}{\rho}\nabla p + \nu\nabla^2\mathbf{u} + \mathbf{g} + \mathbf{f}. \tag{2}$$

Here, $\mathbf{u}$ is the velocity vector, p represents the pressure, $\mathbf{g}$ is the gravity acceleration vector and ν is the kinematic viscosity. The forcing term $\mathbf{f}$ is later defined in order to account for the presence of the net in the fluid domain. Turbulent viscosity is calculated using a k-ω turbulence model and added to ν in Eq. (2).

The system of equations is solved on a rectilinear staggered grid which stores the velocities and velocity related terms such as $\mathbf{f}$ on the cell faces and the pressure in the cell centres. Hence, tight coupling between pressure and velocity is ensured. Finite differences are employed to represent the terms in the Eqns. (1) and (2) in the discrete space. The convection term is discretised with a fifth-order accurate weighted essentially non-oscillatory (WENO) scheme [22] adapted to non-uniform point distances, and for Laplacian terms, second-order accurate central differences are applied. All terms are advanced in time using a third-order accurate TVD Runge-Kutta scheme [23] except the diffusion term, which is handled by the implicit Euler method. This effectively removes the strong restriction on the CFL-number from the diffusion term.

Chorin's projection method for incompressible flows [24] is implemented in REEF3D. First, the predictor step

$$\frac{\mathbf{u}^{(*)} - \mathbf{u}^{(n)}}{\Delta t} = -\mathbf{u}^{(n)} \cdot \nabla\mathbf{u}^{(n)} + \nu\nabla^2\mathbf{u}^{(n+1)} + \mathbf{g} + \mathbf{f}^{(*)}, \tag{3}$$

is solved for the velocities $\mathbf{u}^{(*)}$ without pressure gradients. Then, a Poisson equation is formulated for the pressure

$$\nabla \cdot \left(\frac{1}{\rho}\nabla p^{(n+1)}\right) = \frac{1}{\Delta t}\nabla \cdot \mathbf{u}^{(*)}. \tag{4}$$

Finally, a velocity field respecting the continuity equation is calculated using

$$\mathbf{u}^{(n+1)} = \mathbf{u}^{(*)} - \frac{\Delta t}{\rho}\nabla p^{(n+1)}. \tag{5}$$

An n-halo domain decomposition strategy is implemented in the CFD solver. Here, the domain is split into several subdomains, and data is transferred to neighbouring subdomains using several layers of ghost cells. Convection term containing equations require three layers due to the application of the fifth-order accurate WENO scheme. Otherwise, one layer is sufficient

because of at most second-order accurate spatial discretization schemes. High-performance computation is enabled by using the message passing interface (MPI) for inter-processor communication. This also enables the usage of the fully parallelized BiCGStab algorithm with geometric multigrid preconditioning of the HYPRE library [25] for solving the Poisson equation (4).

NUMERICAL MODEL FOR SOLVING NET DYNAMICS

A typical net in the aquaculture industry consists of a large number of meshes in the form of a porous cylinder or sheet. The resolution of all meshes in a computational simulation would demand too large costs today. Therefore, the net is defined by several larger numerical meshes, and each numerical mesh represents the effect of several physical meshes in the simulation. This is incorporated by utilising the solidity of a porous sheet Sn, [26]

$$Sn = \frac{2d_t}{l_t} - \left(\frac{d_t}{l_t} \right)^2, \tag{6}$$

which defines the ratio of the solid front area to the total area. Here, d_t is diameter of the physical twines and l_t their length. Each numerical mesh is additionally split into four screens, and each screen is assigned to the connected knot.
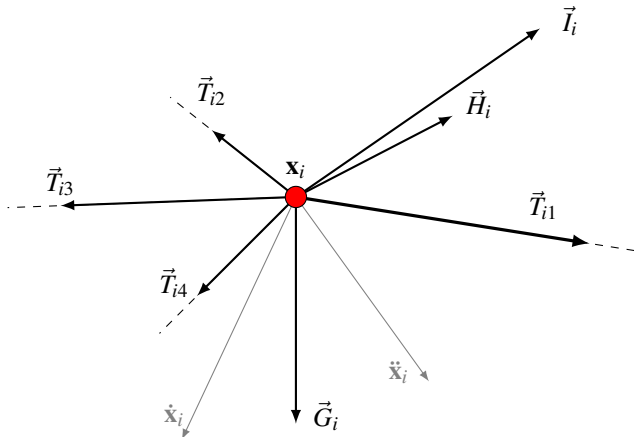

FIGURE 1: ILLUSTRATION OF THE DYNAMIC FORCE EQUILIBRIUM AT THE KNOT $\mathbf{x}_i$.

Following the approach of the screen force model [9], the hydrodynamic forces $\mathbf{H}_i$ of the fluid on the screens with areas A_s around knot i can be calculated as

$$\mathbf{H}_i = \sum_{s=1}^{S_i} \frac{\rho}{2} u_{\text{rel,s}}^2 (c_d \mathbf{n}_d + c_l \mathbf{n}_l)_s \, \mathbf{A}_s, \tag{7}$$

with $\mathbf{n}_d$ the normal and $\mathbf{n}_l$ the tangential direction of the relative velocity vector $\mathbf{u}_{\text{rel,s}} = \mathbf{u}_s - \dot{\mathbf{x}}_s$. They are depended on each other following the relations:

$$\mathbf{n}_{d,s} = \frac{\mathbf{u}_{rel,s}}{|\mathbf{u}_{rel,s}|}, \tag{8}$$

$$\mathbf{n}_{l,s} = \frac{(\mathbf{u}_{rel,s} \times \mathbf{n}_s) \times \mathbf{n}_s}{|(\mathbf{u}_{rel,s} \times \mathbf{n}_s) \times \mathbf{n}_s|}. \tag{9}$$

Here, $\mathbf{n}_s$ is the unit normal vector of the screen pointing in the same direction as $\mathbf{u}_{\text{rel,s}}$. The drag and lift coefficients c_d and c_l are calculated from a truncated Fourier series expanded for the angle of attack α between fluid and screen direction. The Fourier coefficients are determined using non-linear fitting to experimental data.

At each time instance, the dynamic equilibrium between the knots has to be fulfilled. At each knot $\mathbf{x}_i$ with N_i neighbouring knots, this can be written as Newton's second law (see also Fig. 1):

$$m_i \, \ddot{\mathbf{x}}_i = \sum_{k=1}^{N_i} \mathbf{T}_{ik} + \mathbf{G}_i + \mathbf{H}_i. \tag{10}$$

with $\mathbf{G}_i$ the vector of the sum of the gravity and buoyancy force and $\mathbf{T}_{ij}$ the tension force vectors

$$\mathbf{T}_{ij} = T_{ij} \, \mathbf{b}_{ij} = T_{ij} \cdot \left(\frac{\mathbf{x}_j - \mathbf{x}_i}{|\mathbf{x}_j - \mathbf{x}_i|} \right), \tag{11}$$

where T_{ij} represents the tension force magnitude and $\mathbf{b}_{ij}$ is the unit vector of the corresponding bar. Further, the mass is lumped at the knots using

$$m_i = \sum_{s=1}^{S_i} (m_{a,s} + m_{\text{air},s}), \tag{12}$$

with $m_{\text{air},s}$ the mass of the screen in air and $m_{a,s}$ its added mass calculated as the mass of the water volume occupied by the screen. The remaining inertia force is written into $\mathbf{I}_i$ as

$$\mathbf{I}_i = 2m_{\text{air},s}\mathbf{a}_s \tag{13}$$

The system of equations (10) is solved numerically as proposed in [15] to ensure physical connectivity after each time step. The length of the bar between knot $\mathbf{x}_i$ and $\mathbf{x}_j$ is connected by the linear elastic relation

$$l_{ij}^2 = l_{0,ij}^2 \cdot (1 + \kappa \, T_{ij})^2, \tag{14}$$

with $l_{0,ij}$ the original length and κ an elasticity constant. At each time step $(n+1)$, Eq. (14) includes both, the unknown position of the knots and the unknown tension forces. A linearisation is introduced in order to approximate this relation by introducing the incremental increase of the tension forces

$$T^{(n+1)} = T^{(n)} + \Delta T. \tag{15}$$

Assuming small elasticity ($\kappa \ll 1$) and small tension fluctuations ($\Delta T \ll 1$), Eq. (14) yields

$$\left(l_{ij}^{(n+1)} \right)^2 = l_{0,ij}^2 \cdot \left(1 + 2\kappa\, T_{ij}^{(n)} \right). \tag{16}$$

In each time step, the kinematic compatibility equation

$$\left(\mathbf{x_j}^{(n+1)} - \mathbf{x_i}^{(n+1)} \right)^2 = \left(l_{ij}^{(n+1)} \right)^2, \tag{17}$$

has to hold for all knots. This can be ensured by solving this equation instead of the dynamic equilibria of Eq. (10). These equilibria are then fulfilled by inserting them into the compatibility equation using finite differences in time for replacing position vectors with accelerations. In this paper, first-order backward finite differences are applied in order to maintain linearity of the problem. They are inserted in the left-hand side of Eq. (17). Finally, the arising terms are linearised such that a system of linear equations is given under consideration of (16):

$$\frac{l_{0,ij}^2}{2\Delta t} \cdot \left(1 + 2\kappa\, T_{ij}^{(n+1)} \right) - \frac{\left(\mathbf{x}_j^{(n)} - \mathbf{x}_i^{(n)} \right)^2}{2\Delta t} = \left(\dot{\mathbf{x}}_{\mathbf{j}}^{(n)} - \dot{\mathbf{x}}_{\mathbf{i}}^{(n)} + \Delta t \left(\ddot{\mathbf{x}}_j^{(n)} - \ddot{\mathbf{x}}_i^{(n)} \right) \right) \left(\mathbf{x}_j^{(n)} - \mathbf{x}_i^{(n)} \right). \tag{18}$$

This can be written for the tension force magnitudes using the definition (11) and Eq. (10):

$$\left(\sum_{k=1}^{N_j} \frac{\mathbf{b}_{jk}^{(n)} T_{jk}^{(n+1)}}{m_j} - \sum_{k=1}^{N_i} \frac{\mathbf{b}_{ik}^{(n)} T_{ik}^{(n+1)}}{m_i} \right) \left(\mathbf{x}_j^{(n)} - \mathbf{x}_i^{(n)} \right)$$

$$- \frac{l_{0,ij}^2}{\Delta t^2} \kappa\, T_{ij}^{(n+1)} = \frac{l_{0,ij}^2}{2\Delta t^2} - \frac{\left(\mathbf{x}_j^{(n)} - \mathbf{x}_i^{(n)} \right)^2}{2\Delta t^2}$$

$$- \frac{\left(\dot{\mathbf{x}}_{\mathbf{j}}^{(n)} - \dot{\mathbf{x}}_{\mathbf{i}}^{(n)} \right) \left(\mathbf{x}_j^{(n)} - \mathbf{x}_i^{(n)} \right)}{\Delta t}$$

$$- \frac{\left(\mathbf{x}_j^{(n)} - \mathbf{x}_i^{(n)} \right) \mathbf{F}_j^{(n)}}{m_j} + \frac{\left(\mathbf{x}_j^{(n)} - \mathbf{x}_i^{(n)} \right) \mathbf{F}_i^{(n)}}{m_i}. \tag{19}$$

The resulting system matrix is inverted using the partially pivoted LU decomposition of the C++ library Eigen [27]. Once a converged result has been found for the tension forces, acceleration, velocity and position of the knots are found from Eq. (10) and

$$\dot{\mathbf{x}}^{(n+1)} = \dot{\mathbf{x}}^{(n)} + \Delta t\, \ddot{\mathbf{x}}^{(n+1)}, \tag{20}$$

$$\mathbf{x}^{(n+1)} = \mathbf{x}^{(n)} + \Delta t\, \dot{\mathbf{x}}^{(n+1)}. \tag{21}$$

As initial conditions, the geometrical information of the net at the start of the simulation has to be given. An efficient algorithm is ensured by storing connectivity matrices as proposed in [13].

WEAK COUPLING OF FLUID AND NET DYNAMICS

The interaction between fluid and net is handled implicitly using a forcing term in the Navier-Stokes equations. This term adds or removes the momentum initiated from the net motion and the porosity of the net. The information is distributed on the numerical grid using an inverse distance weighting interpolation. For this purpose, the term $\mathbf{f}$ in Eq. (3) is approximated at point $\mathbf{x}_e$ of the fluid grid using

$$\mathbf{f}(\mathbf{x}_e) = \frac{1}{\kappa} \cdot \frac{\sum_{l=1}^{L} w_{e,l} \cdot \tilde{\mathbf{f}}(\mathbf{x}_l)}{\sum_{l=1}^{L} w_{e,l}}, \tag{22}$$

with $\tilde{\mathbf{f}}(\mathbf{x}_l)$ the hydrodynamic screen force vector at the point $\mathbf{x}_l$ on the net, L the number of knots on the net within a defined Kernel around $\mathbf{x}_e$ and $w_{e,l}$ the dimensionless weights chosen as

$$w_{e,l} = \frac{1}{|\mathbf{x}_e - \mathbf{x}_l|^2}. \tag{23}$$

The parameter κ arises in (22) from the transition of a surface force to a volume force and represents the diameter of the influence sphere of each knot. It is adjusted so that it accurately predicts the deceleration of the flow through the net. Finally, the screen forces are represented by the drag and lift forces at each knot (Eq. (7)):

$$\tilde{\mathbf{f}}(\mathbf{x}_l) = \frac{\rho}{2} u_{\mathrm{rel},l}^2 \cdot \left(c_d \mathbf{n}_d + c_l \mathbf{n}_l \right)_l. \tag{24}$$

It is noticed that the same interpolation procedure is used to obtain the fluid velocities for the calculation of the hydrodynamic forces on the net screens u_s.

VALIDATION OF THE NUMERICAL MODEL

Several validation cases are presented for the proposed numerical model. In particular, forces on net sheets, their deformation and the velocity reduction behind them are compared to available experimental data.

The decrease of velocity is typically indicated by the velocity reduction factor U_r

$$U_r = 1.0 - \frac{u_w}{u_\infty}, \qquad (25)$$

with u_w the velocity in the wake of the net. Further, the numerically predicted forces on the net are determined by integrating (7) over the net surface.

Forces on a fixed net panel

First, the accuracy of the drag force estimation of the proposed numerical model is investigated. For this purpose, the experimental data of Rudi et al. [28] is considered. They measured the drag forces on a fixed net panel in a steady current using varying inflow velocities u_∞, angles of attack α and net geometries.
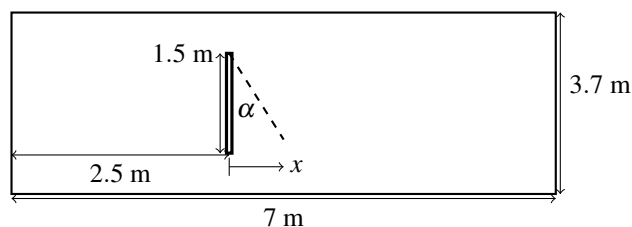
FIGURE 2: COMPUTATIONAL DOMAIN FOR THE SIMULATION OF THE FIXED NET PANEL IN STEADY CURRENT FLOW BY RUDI ET AL. [28]. THE DOMAIN IS SYMMETRICAL IN Y- AND Z-DIRECTION.

The net with solidities $Sn = 0.13$ and 0.243 is fixed in a neglected frame of 1.5 m × 1.5 m. The angles of attack are $\alpha = 0°, 30°$ and $60°$ with α defined as shown in Fig. 2. The inflow velocities are 0.159 m/s, 0.316 m/s and 0.966 m/s. As the computational domain, a 7 m long and 3.7 m wide and high rectangular box is considered, and the net is placed in the middle of the domain at $x = 2.5$ m. The size of the domain is chosen so that the results are not influenced by the boundaries of the domain. As results, Fig. 3 shows the comparison of the drag force coefficients between the experimental data and the numerical predictions.

Fig. 3a presents the numerical and experimental drag force coefficients for the different inflow velocities as a function of α for $Sn = 0.13$. The computed drag coefficients decrease with increasing inflow velocity and increasing angle of attack. This
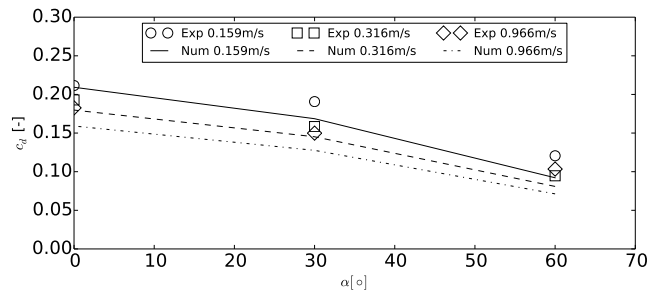
(a) $Sn = 0.13$.
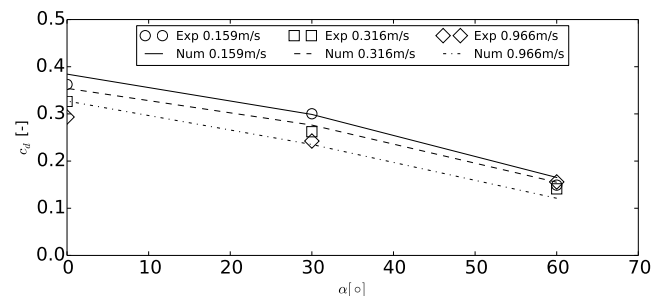
(b) $Sn = 0.243$.

FIGURE 3: COMPARISON OF THE NUMERICAL AND EXPERIMENTAL DRAG FORCE COEFFICIENTS FOR THE FIXED NET PANEL IN DIFFERENT STEADY CURRENT FLOWS AND DIFFERENT ANGLES OF ATTACK.

agrees qualitatively with the measurements. The smallest deviations can be found for $u_\infty = 0.316$ m/s, whereas the model under-predicts c_d for smaller and larger velocities by up to 30%. Similar results are shown for $Sn = 0.243$ in Fig. 3b. Generally, a better agreement between experiments and simulation is stated. The maximum deviation occurs for $\alpha = 0°$ and $u_\infty = 0.966$ m/s with 22% over-prediction.

It is noticed that the numerical model includes empirical approximations for c_d which are obtained from experimental data. A better agreement could hence be obtained if the incorporated data set would be limited to the measurements for this particular net sheet.

Velocity reduction behind a fixed net panel

In the experiments of Bi et al. [29], PIV measurements of the fluid around a single and multiple fixed net panels in varying currents were performed. The flume is 22 m long, 0.45 m wide, 0.6 m high and has a water depth of 0.4 m. Amongst other investigations, a single fixed net panel of 0.3 m × 0.3 m is placed in the centre of the flume normal to the flow direction. Three different net configurations are investigated with varying solidity of $Sn = 0.135, 0.243$, and 0.272. The inflow velocities u_∞ are 0.056 m/s, 0.113 m/s, 0.17 m/s and 0.226 m/s. The presence of

the net panel extracts momentum from the fluid which results in a flow velocity reduction as illustrated in Fig. 4. The accurate determination of this reduction is of major importance for modelling the flow pattern in the cage and the loads on the back side of the structure. In the experiments, the fluid velocity was measured one frame length L behind the net for each geometry. Additionally, the velocity profile along a line in x-direction through the centre of the net was reported for $u_\infty = 0.17$ m/s. The comparability of the numerically calculated velocities at specific points of the physical experiment is not valid because of the continuous numerical representation of the net in the fluid domain. Therefore, velocity probes are arranged in the form of a disc around the measured point and the average value is compared with that from the experiment. This should provide a better impression of the numerical accuracy because it takes the discrete approach of macro elements into account.
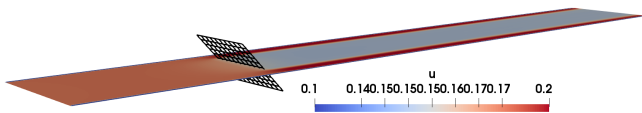
FIGURE 4: NUMERICALLY CALCULATED X-VELOCITY DISTRIBUTION ON X-Y PLANE THROUGH THE CENTRE OF THE NET FOR THE CONFIGURATION $Sn = 0.243$, $u_\infty = 0.17$ m/s AND $\alpha = 45°$.

The computational domain is shown in Fig. 5. The tank has the dimensions 4 m × 0.5 m × 0.5 m, and the net panel is placed centred at $x = 1.5$ m. As the results, the velocity reduction factor U_r is compared for the different net geometries and varying angles of attack between $0°$ and $60°$ in Fig. 6 and 7.
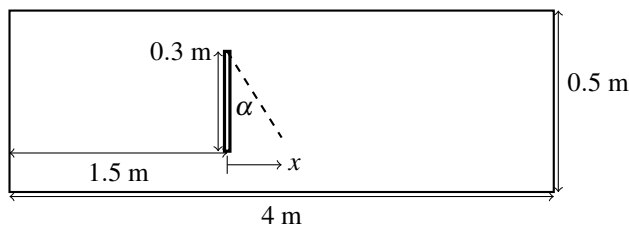

FIGURE 5: COMPUTATIONAL DOMAIN FOR THE SIMULATION OF THE FIXED NET PANEL IN STEADY CURRENT FLOW BY BI ET AL. [29]. THE DOMAIN IS SYMMETRICAL IN Y- AND Z-DIRECTION.

Fig. 6a shows U_r over u_∞ two L behind the net located perpendicular to the inflow. The relative velocity reduction increases

with the solidity of the net due to increased shielding. Further, U_r only slightly decreases with increased inflow velocity, expect of the smallest velocity where a strong increase is measured for two of the nets. It is to be discussed whether this deflection is due to physical effects or uncertainty sensitivity which amplifies at this point due to the small flow velocity and the division by u_∞ in Eq. (25). Exempt from these data points, the numerical model shows a very good agreement with the experiments as the deviations are mostly below 10%. Fig. 6a provides further insight by showing the distribution of U_r over x on the middle line through the net. Here, the experiments show a slight decrease of U_r over x behind the net. This effect implies an acceleration of the fluid which might be due to enhanced turbulence in the wake-field. In the numerical model, this would have to be incorporated by increasing the turbulence production through the net in the turbulence model. Despite this, the simulations can still provide an accurate distribution with all errors below 10%.
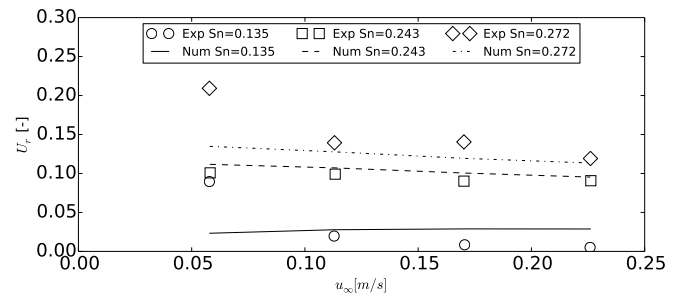
(a) VELOCITY REDUCTION FACTORS AT $x/L = 2.0$ OVER VARYING INFLOW VELOCITIES.
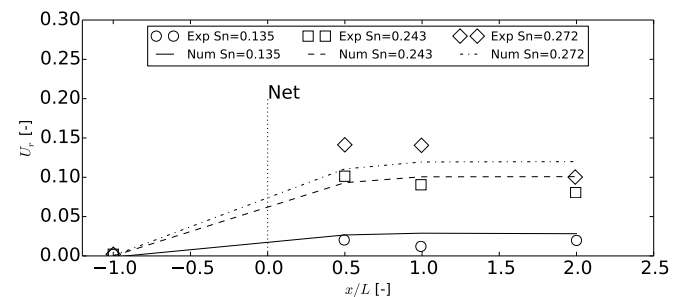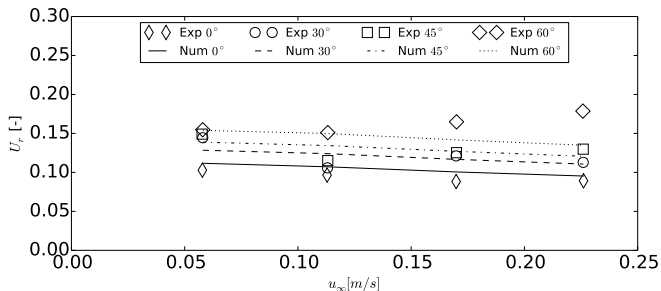

(b) DISTRIBUTION OF THE VELOCITY REDUCTION FACTORS ALONG THE MIDDLE LINE THROUGH THE NET PANEL FOR $u_\infty = 0.17$ m/s.
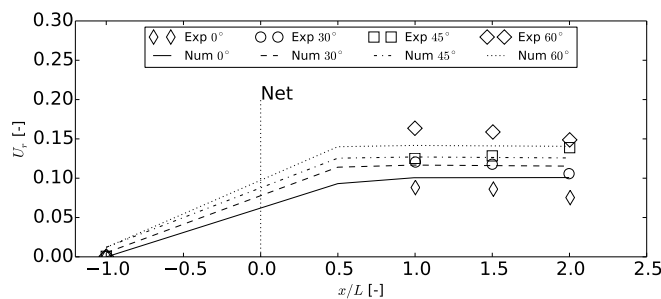
FIGURE 6: COMPARISON OF THE NUMERICAL AND EXPERIMENTAL PREDICTED VELOCITY REDUCTION FACTORS FOR VARYING SOLIDITIES AND $\alpha = 0°$.

The net with solidity $Sn = 0.243$ is further analysed by varying the angle of attack with the inflow. In Fig. 7a, U_r over u_∞ two L

behind the net located perpendicular to the inflow is shown for $\alpha = 0° - 60°$. Physically, the reduction factor increases with α due to the increasing net area perpendicular to the flow. Further, the factor decreases with increasing inflow velocity for small α but increases with increasing inflow velocity for larger angles. The model accurately reproduces the first effect but cannot reproduce the increase of U_r over u_∞ for $\alpha = 60°$. For the distribution of U_r over x (Fig. 7b), similar agreement as above can be found between experiment and simulation.

(a) VELOCITY REDUCTION FACTORS AT $x/L = 2.0$ OVER VARYING INFLOW VELOCITIES.

(b) DISTRIBUTION OF THE VELOCITY REDUCTION FACTORS ALONG THE MIDDLE LINE THROUGH THE NET PANEL FOR $u_\infty = 0.17$ m/s.

FIGURE 7: COMPARISON OF THE NUMERICAL AND EXPERIMENTAL PREDICTED VELOCITY REDUCTION FACTORS FOR $Sn = 0.243$ AND VARYING ANGLES OF ATTACK.

Deformation of a single net panel in steady current

After the validation of the force model and coupling algorithm, the net deformation is included for a final validation case. Bi et al. [4] conducted experiments on a flexible net sheet in a similar configuration as presented in the previous section. The net of 0.3 m $\times 0.3$ m has a solidity of 0.243, and a steel bar with a mass of 64.5 g in water is attached to the bottom of the net. The bar is not resolved in the simulation but added as additional masses

to the first row of meshes. The computational domain is taken from above (see Fig. 5). The inflow velocities u_∞ are 0.056 m/s, 0.113 m/s, 0.17 m/s and 0.226 m/s. The interaction of fluid and net results in the deformation of the net and a velocity reduction in its wake as shown in Fig. 8.
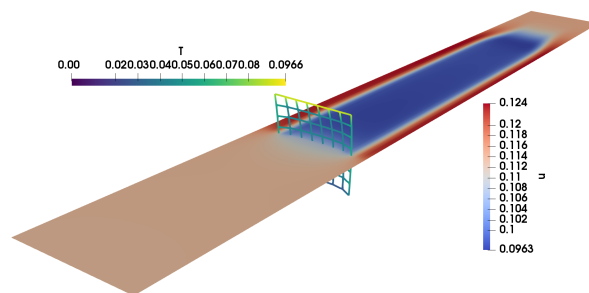

FIGURE 8: NUMERICALLY CALCULATED X-VELOCITY DISTRIBUTION ON X-Y PLANE THROUGH THE CENTRE OF THE NET FOR $u_\infty = 0.113$ m/s.

First, the deformation of the net is compared with experimental data extracted from pictures during the measurements in Fig. 9. Generally, the numerical model provides an accurate representation of the physical deformation over the whole range of inflow velocities. For larger velocities, the model tends to predict a larger curvature in the middle part of the net so that the lowest point deflects less in comparison to the experiment.
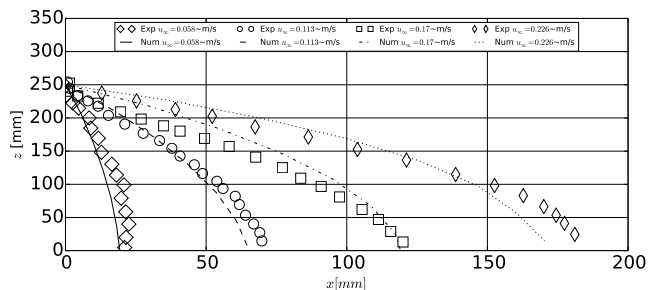

FIGURE 9: COMPARISON OF THE DEFORMATION OF THE NET. THE FIGURE SHOWS THE DISTRIBUTION OF THE NET IN THE X-Z PLANE THROUGH ITS CENTRE FOR THE DIFFERENT INFLOW VELOCITIES.

Next, the total drag forces on the deformed net are analysed in Fig. 10. For the numerical results, the forces on the sinker are approximated using Morison forces on a cylinder. The drag forces increase quadratically with the velocity as expected, and the numerical model shows good agreement with the experiments for lower inflow velocities. The deviations increase with the inflow velocity which might be due to the increasing importance of the forces on the sinker. Fig. 11 shows the distribution of the velocity reduction factor behind the net for two inflow velocities. The general distribution of U_r and agreement between experiment and numerical model is, as expected, similar to above. The maximum deviation occurs at $x/L = 2$ with an over-prediction of 7%.

APPLICATION TO MULTIPLE DEFORMING NET PANELS IN STEADY CURRENT

In the following, the study of the interaction of current flow and four deforming net panels is presented. This shall emphasise the advantage of the presented model to simulate the interaction of several nets with each other within a single fluid domain. The setup is the same as reported in [29], but the deformation of the nets is enabled. The computational domain is shown in Fig. 12. Three additional nets are added behind the original net with a distance of one frame length between each of them. The inflow velocity is chosen as $u_\infty = 0.17$ m/s. In the simulation, about 3% of the total computational time is linked to a single net calculation and its coupling to the fluid solver. Fig. 13 shows the resulting flow pattern around the nets and the net deformation at steady state.

FIGURE 10: COMPARISON OF THE TOTAL DRAG FORCES ON THE DEFORMED NET OVER THE INFLOW VELOCITIES.

FIGURE 12: COMPUTATIONAL DOMAIN FOR THE SIMULATION OF FOUR DEFORMING NET PANELS IN STEADY CURRENT FLOW. THE DOMAIN IS SYMMETRICAL IN Y- AND Z-DIRECTION.
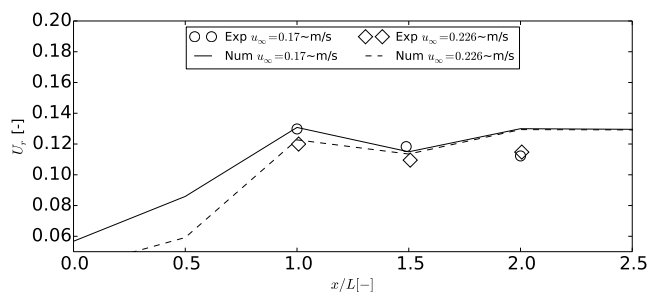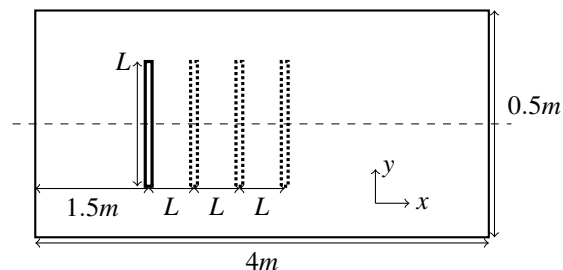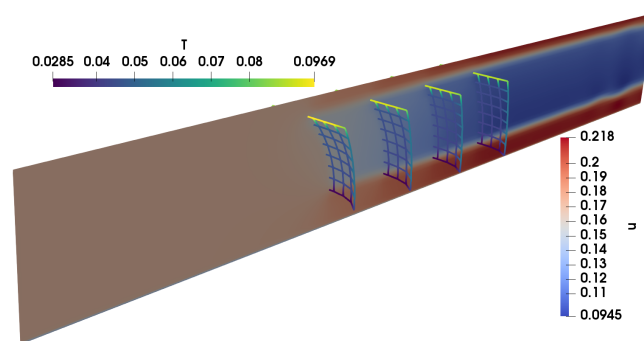

FIGURE 11: COMPARISON OF THE DISTRIBUTION OF THE VELOCITY REDUCTION FACTORS ALONG THE MIDDLE LINE THROUGH THE NET PANEL ($x/L \approx 0$).

FIGURE 13: NUMERICALLY CALCULATED X-VELOCITY DISTRIBUTION ON X-Y PLANE THROUGH THE CENTRE OF THE DEFORMED NETS.

In Fig. 14, the deformation of the $N = 4$ nets is shown. The

net in the front deforms the most due to the undisturbed inflow conditions. The deformations of the downstream nets reduce successively due to the velocity reduction through each structure as indicated in Fig. 15. It is further noticeable that downstream nets slightly influence the flow through upstream panels due to impounded water. Finally, Fig. 16 shows the total drag forces on each of the nets. The reduced inflow velocity results in reduced drag forces on the downstream structures as expected. Between the first and last net, a reduction of 40% is calculated.
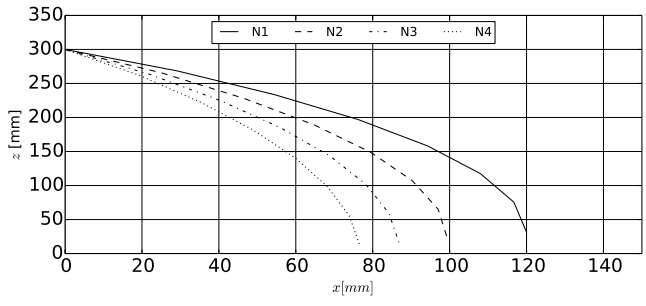

FIGURE 16: NUMERICAL TOTAL DRAG FORCES ON THE DEFORMED NETS.

FIGURE 14: NUMERICAL DEFORMATION OF THE NETS SHOWN AS THE DISTRIBUTION OF THE NETS IN THE X-Z PLANE THROUGH ITS CENTRES.

screen force model. This model has advantages over Morison type force models due to the incorporation of the angle between fluid and net into its formulation. An implicit model is chosen for the calculation of the net dynamics to avoid time-step restrictions or sub-step iterations in the fluid solution. Hence, the inclusion into existing CFD solvers is straightforward and the effect on the efficiency of the solver is minimised.

The numerical model is validated against existing experiments for fixed and deforming net panels with varying geometries and solidities in current flows. Overall, the proposed model agrees well with the experimental data as most deviations for drag forces and velocity reduction are below 10%. It is noticed that the numerical model relies on empirical data for the drag force on a net panel. Therefore, the quality and quantity of available experimental data influences the results of the CFD model. The study of multiple deforming nets delivers insight into possible applications and advantages of the model. Future work will focus on the simulation of fish cages in current and waves and the inclusion of free surfaces with a moving collar.
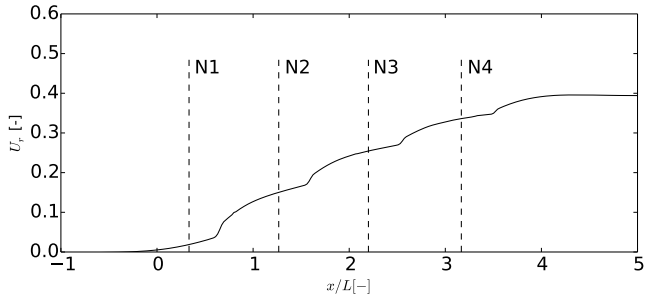

FIGURE 15: NUMERICAL DISTRIBUTION OF THE VELOCITY REDUCTION FACTOR ALONG THE MIDDLE LINE THROUGH THE NET PANELS.

CONCLUSION

The present paper describes a complete numerical model for simulating the interaction of deforming nets and fluid dynamics. The coupling is achieved through the inclusion of the momentum disturbances in the Reynolds-averaged Navier-Stokes equations. The forces on the net are calculated under the usage of the
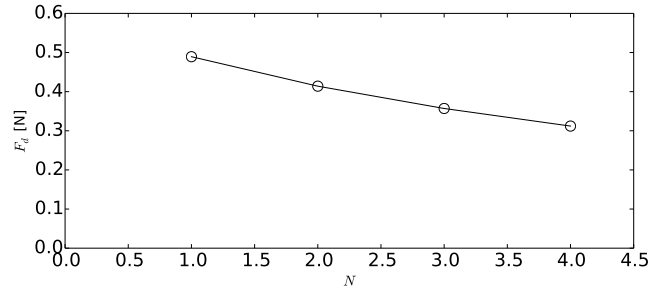
REFERENCES

[1] Løland, G., 1991. Current forces on and flow through fish farms. Ph.D. thesis, NTH Trondheim, Norway.

[2] Kristiansen, T., and Faltinsen, O. M., 2015. "Experimental and numerical study of an aquaculture net cage with floater in waves and current". *Journal of Fluids and Structures,* **54**, pp. 1–26.

[3] Patursson, Ø., Swift, M. R., Tsukrov, I., Simonsen, K.,

Baldwin, K., Fredriksson, D., and Celikkol, B., 2010. "Development of a porous media model with application to flow through and around a net panel". *Ocean Engineering, 37*, pp. 314–324.

[4] Bi, C.-W., Zhao, Y.-P., Dong, G.-H., Xu, T.-J., and Gui, F.-K., 2014. "Numerical simulation of the interaction between flow and flexible nets". *J. Fluids Struct., 45*, pp. 180–201.

[5] Zhao, Y.-P., Bi, C.-W., Liu, Y.-X., Dong, G.-H., and Gui, F.-K., 2014. "Numerical Simulation of Interaction Between Waves and Net Panel Using Porous Media Model". *Engineering Applications of Computational Fluid Mechanics, 8*(1), pp. 116–126.

[6] Chen, H., and Christensen, E., 2016. "Investigations on the porous resistance coefficients for fishing net structures". *J. Fluids Struct., 65*, pp. 76–107.

[7] Chen, H., and Christensen, E., 2017. "Development of a numerical model for fluid-structure interaction analysis of flow through and around an aquaculture net cage". *Ocean Engineering, 142*, pp. 597–615.

[8] Martin, T., Kamath, A., and Bihs, H., 2019. *Numerical Modelling of the Interaction between a Fish Net and Fluid using CFD*. Proceedings of VII International Conference on Computational Methods in Marine Engineering, MARINE 2019, Gothenburg, Sweden.

[9] Kristiansen, T., and Faltinsen, O. M., 2012. "Modelling of current loads on aquaculture net cages". *Journal of Fluids and Structures, 34*, p. 218–235.

[10] Tsukrov, I., Eroshkin, O., Fredriksson, D., Swift, M., and Celikkol, B., 2003. "Finite element modeling of net panels using a consistent net element". *Ocean Engineering, 30*, p. 251–270.

[11] Lader, P. F., and Fredheim, A., 2006. "Dynamic properties of a flexible net sheet in waves and current—A numerical approach". *Aquacultural Engineering, 35 (3)*, p. 228–238.

[12] Bi, C.-W., Zhao, Y.-P., Dong, G.-H., Zheng, Y.-N., and Gui, F.-K., 2014. "A numerical analysis on the hydrodynamic characteristics of net cages using coupled fluid–structure interaction model". *Aquaculture Engineering, 59*, pp. 1–12.

[13] Martin, T., Schacht, S., Riesen, P., and Paschen, M., 2018. "Efficient implementation of a numerical model for flexible net structures". *Ocean Engineering, Volume 150*, pp. 272 – 279.

[14] LeBris, F., and Marichal, D., 1998. "Numerical and experimental study of submerged supple nets applications to fish farms". *Journal of Marine Science Technology, 3*, pp. 161–170.

[15] Marichal, D., 2003. *Cod-end numerical study*. In: Proceedings of the 3rd International Conference on Hydroelasticity in Marine Technology, Oxford, UK.

[16] Bihs, H., Kamath, A., Alagan Chella, M., Aggarwal, A., and Arntsen, Ø. A., 2016. "A new level set numerical wave tank with improved density interpolation for complex wave hydrodynamics". *Computers & Fluids, Volume 140*, pp. 191–208.

[17] Kamath, A., Chella, M. A., Bihs, H., and Arntsen, O. A., 2017. "Energy transfer due to shoaling and decomposition of breaking and non-breaking waves over a submerged bar". *Engineering Applications of Computational Fluid Mechanics, Volume 11(1)*, pp. 450–466.

[18] Kamath, A., Chella, M. A., Bihs, H., and Arntsen, O. A., 2015. "Evaluating wave forces on groups of three and nine cylinders using a 3D numerical wave tank". *Engineering Applications of Computational Fluid Mechanics, Volume 9*, pp. 343–354.

[19] Grotle, E. L., Bihs, H., and Æsøy, V., 2017. "Experimental and numerical investigation of sloshing under roll excitation at shallow liquid depths". *Ocean Engineering, Volume 138*, pp. 73–85.

[20] Bihs, H., and Kamath, A., 2017. "A combined level set/ghost cell immersed boundary representation for floating body simulations". *Int. J. Numer. Meth. Fluids, Volume 83*, pp. 905–916.

[21] Martin, T., Kamath, A., and Bihs, H., 2019. "Modeling and Simulation of Moored-Floating Structures Using the Tension Element Method". *Journal of Offshore Mechanics and Arctic Engineering, 142 (1)*.

[22] Jiang, G., and Shu, C., 1996. "Efficient implementation of weighted ENO schemes". *Journal of Computational Physics, Volume 126(1)*, pp. 202–228.

[23] Shu, C., and Osher, S., 1988. "Efficient implementation of essentially non-oscillatory shock-capturing schemes". *Journal of Computational Physics, Volume 77(2)*, pp. 439–471.

[24] Chorin, A., 1968. "Numerical solution of the Navier-Stokes equations". *Mathematics of Computation, Volume 22*, pp. 745–762.

[25] van der Vorst, H., 1992. "BiCGStab: A fast and smoothly converging variant of Bi-CG for the solution of nonsymmetric linear systems". *SIAM Journal of Scientific Computing, Volume 13*, pp. 631–644.

[26] Fredheim, A., 2005. Current Forces on Net Structures. Ph.D. thesis, NTNU Trondheim, Norway.

[27] Guennebaud, G., Jacob, B., et al., 2010. Eigen v3. http://eigen.tuxfamily.org.

[28] Rudi, H., Løland, G., and Furunes, I., 1988. Experiments With Nets; Forces on and Flow Through Net Panels and Cage Systems. Technical Report MT51 F88-0215, MARINTEK, Trondheim, Norway.

[29] Bi, C.-W., Zhao, Y.-P., Dong, G.-H., Xu, T.-J., and Gui, F.-K., 2013. "Experimental investigation of the reduction in flow velocity downstream from a fishing net". *Aquaculture Engineering, 57*, pp. 71–81.